This is a peer-reviewed, post-print (final draft post-refereeing) version of the following published document, This is the peer reviewed version of the following article: [FULL CITE], which has been published in final form at https://doi.org/10.1002/esp.4693. This article may be used for non-commercial purposes in accordance with Wiley Terms and Conditions for Self-Archiving. and is licensed under All Rights Reserved license:

Mol, Lisa ORCID logoORCID: https://orcid.org/0000-0001-5272-3671 and Clarke, Lucy E ORCID logoORCID: https://orcid.org/0000-0002-8174-3839 (2019) Integrating structure-from-motion photogrammetry into rock weathering field methodologies. Earth Surface Processes and Landforms, 44 (13). pp. 2671-2684. doi:10.1002/esp.4693

Official URL: https://doi.org/10.1002/esp.4693
DOI: http://dx.doi.org/10.1002/esp.4693
EPrint URI: https://eprints.glos.ac.uk/id/eprint/6966

Disclaimer

The University of Gloucestershire has obtained warranties from all depositors as to their title in the material deposited and as to their right to deposit such material.

The University of Gloucestershire makes no representation or warranties of commercial utility, title, or fitness for a particular purpose or any other warranty, express or implied in respect of any material deposited.

The University of Gloucestershire makes no representation that the use of the materials will not infringe any patent, copyright, trademark or other property or proprietary rights.

The University of Gloucestershire accepts no liability for any infringement of intellectual property rights in any material deposited but will remove such material from public view pending investigation in the event of an allegation of any such infringement.

PLEASE SCROLL DOWN FOR TEXT.

Mol Lisa (Orcid ID: 0000-0001-5272-3671)

Clarke Lucy (Orcid ID: 0000-0002-8174-3839)

Integrating Structure from Motion photogrammetry into rock weathering field methodologies

Lisa Mol[1]. Lucy Clarke[2]

[1] Department of Geography and Environmental Management, University of the West of England. Frenchay Campus, Coldharbour Lane, Bristol, BS16 1QY, UK. lisa.mol@uwe.ac.uk +447825678390

[2] Department of Geography, University of Gloucestershire Cheltenham, UK.

Abstract

Despite recent rapid advances in the field of Structure from Motion (SfM) photogrammetry, the use of high-resolution data to investigate small scale processes is a relatively underdeveloped field. In particular, rock weathering is rarely investigated using this suite of techniques. This research uses a combination of traditional non-destructive rock weathering measurement techniques (rock surface hardness) and SfM to map deterioration and loss of cohesion of the surface using 3-dimensional data. The results are used to interpret weathering behaviour across two different lithologies present on the site, namely shale and limestone. This new approach is tested on seven sites in Longyearbyen, Svalbard, where active weathering of a rock surface was

This article has been accepted for publication and undergone full peer review but has not been through the copyediting, typesetting, pagination and proofreading process which may lead to differences between this version and the Version of Record. Please cite this article as doi: 10.1002/esp.4693

measured after 13 years of exposure to extreme temperature regimes and snow cover. The surface loss was quantified with SfM and combined with rock surface hardness measurement distributions extrapolated in GIS. The combined results are used here to quantify the difference in response of both lithologies to these extreme temperatures. This research demonstrates the potential for further integration of SfM in rock weathering research and other small-scale geomorphological investigations, in particular in difficult field conditions where portability of field equipment is paramount.

Keywords: rock weathering, Structure from Motion, rock hardness, surface roughness, Arctic

Introduction

Since the development of Structure from Motion (SfM), photogrammetry has been increasingly used in geomorphological studies to map changes on landscape scales (Westoby *et al*, 2012; Piermattei *et al*, 2015; Smith *et al*, 2016). These insights have been invaluable in processing rates of change and increasing our understanding of landscape dynamics. For example, SfM has brought to light the potential for these relatively low-cost methods to supplement, or even compete with, more expensive methods such as laser scanning in fluvial (Fonstad *et al*, 2013; Javernick *et al*, 2014, Dietrich, 2016), coastal (Mancini *et al*, 2013), glacial (Tonkin *et al*, 2014) and erosion (Smith and Vericat, 2015) investigations. Recent advances include everyday technology such as consumer-level cameras (James and Robson, 2012) and smart phones (Micheletti *et al*, 2015), thus enhancing accessibility of this method even at undergraduate level (Williams *et al*, 2017). This has enabled increasingly targeted high-resolution studies of change in landform morphology in response to climatic events such as bank erosion and associated volumetric loss analysis (Barker *et al*, 1997; Fonstad *et al*, 2013), and coastal changes (Adams and Chandler, 2002; Mancini *et al*, 2013). Further advances in the automation of the data processing and interpolation has further increased the accuracy and ease of use of SfM as a geomorphological tool (Westaway *et al*, 2000; Westoby *et al*, 2012; Smith *et al*, 2016). However, in order to ensure the accuracy and usability of the final digital surface models produced by SfM it has been demonstrated that the internal self-calibration bundle used within the software is not sufficient alone to remove image distortion and reference points with a specific location/coordinate in space are required to reduce these errors (Barry and Coakley, 2013; James and Robson, 2014; Tonkin and Midgley, 2016). In conjunction with commercialisation of unmanned aerial vehicles (UAVs), this method can now provide an accessible means of generating 3-dimensional (3D) terrain models and monitoring landscape change, such as fluvial migration and erosion, in specific target areas and reduces the need to engage with relatively expensive techniques such as lidar surveys (Cook, 2017). Furthermore, where historic aerial photography is available it is possible to reconstruct landscape change over a longer temporal scale, such as decades rather than years (Schiefer and Gilbert, 2007).

The use of photogrammetry to monitor rock weathering, however, has not seen a surge similar to that experienced by other landscape development disciplines, despite 3D mapping of surfaces having been used for cliff-scale (10s - 100s meters) studies as well as at smaller scales under controlled laboratory conditions (James and Robson, 2012; Brasington, 2003) and for photo-sieving on a patch scale (Westoby *et al*, 2015). Research addressing rock weathering at the microscale largely still relies on traditional methods such as Rock Surface Hardness (RSH) (Betts and Latta, 2000; Viles *et al*, 2011; Mol and Viles, 2012), moisture meters (Matsukura and Takahashi, 2000; Eklund *et al*, 2013), temperature loggers (Hall and André, 2001; Sumner *et al*, 2004; McKay *et al*, 2009; Mol and Viles, 2010) and micromorphological changes to the surface measured in the laboratory (Smith and McGreevy, 1988; Zhu *et al,* 2003; Gomez-Heras and Fort, 2007; Bourke *et al*, 2008). While these investigations have advanced the field of weathering science significantly, there remain difficulties with the use of photogrammetry in the field at a sufficiently high resolution to monitor rock weathering at a meaningful scale. In particular, the absence of lightweight photogrammetric equipment that can be used with equally portable rock weathering equipment has led to an absence of in-field 3D analysis at a scale appropriate to the weathering studies aforementioned; something that can now addressed with the use of SfM. This could be of particular use at sites which are difficult to reach and/or subjected to extreme temperature regimes, such as the site investigated here. Often it is not possible to carry heavier equipment (for example 3D scanners with tripods) up to challenging field sites such as exposed rock outcrops at the tops of slopes, sites that are a substantial distance from the nearest road or even sites such as busy pavements where it is difficult to set up measuring equipment.

This research explores the potential for high resolution SfM photogrammetry to assess weathering rates on a friable shale and sandstone stratigraphy using a commercially available Bridge SLR camera (Fujifilm FinePix SL300). This low-cost approach not only represents a potential advancement in weathering studies but also further integrates equipment accessible to researchers into the suite of available methodologies for carrying out weathering projects. The site presented contains a complex lithology, alternating bands of shale and sandstone, and is exposed to freezing temperatures (<0^0C) for at least seven to eight months a year. Previous research on polar environmental weathering has shown the importance of freeze-thaw weathering (Hall and André, 2001), driven by the availability of moisture during the summer seasons (Matsuoka, 1995), as well as the influence of the extreme thermal regime itself through thermal fatigue and shock (Sumner *et al*, 2004). In this study we investigate the potential for integration of SfM to observe differential response of composite lithology sites through quantification of the relative loss of material per lithological band as well as corresponding rock surface hardness and roughness values. The case study presented here illustrates the use of conventional rock weathering equipment together with a novel application of SfM to present a new methodological opportunity. It does not purport to be a detailed weathering study of Arctic lithologies but instead illustrates how the method presented here can be used to observe differential behaviour in rock weathering. In this case study we investigate the function of lithology under homogenous conditions (i.e. similar exposure to temperature fluctuations, salt movement etc).

Field site

Longyearbyen is the northernmost permanently inhabited settlement at 78°13′ N, 15° 47′ E, situated in the mountainous archipelago of Svalbard in the High Arctic (Eckerstorfer and Christiansen, 2011). The town itself is situated in Longyeardalen, a U-shaped valley joining the plain of Adventdalen before reaching Isfjorden (see figure 1). This area predominantly consists of Early Cretaceous sandstones, conglomerates, clay ironstones, shales and coal of the Carolinefjellet Formation (Harris *et al*, 2011). The experimental site is located on a cutting in the fragile shales, interspersed with bands of sandstones, which facilitates the road from the main town to the airport

(78.2274^{0}N, 15.5992^{0}E) situated on the marine deposits reaching into Isfjorden to the northwest of Longyearbyen (see figure 2A).

Figure 1: Location map showing the study site (indicated by a star) new Longyearbyen, Svalbard

Figure 2: [A] Overview photo of the experimental site, [B] water runoff channel, includes sites 6 and 7

The site is relatively sheltered, and can reach near-surface temperatures into the high twenty degrees (see figure 3) in the afternoon during summer, as recorded by onsite high-resolution temperature loggers (MadgeTech Temp1000IS). It is likely that this is a reflection of the sheltered nature of the site as well as reflection of heat off the lighter sandstone surfaces and is higher than the reported ambient temperatures; the reported peak in temperature on the 7th of July 2015 of 28.4^{0}C corresponds with a reported high of 10.5^{0}C at the more exposed Svalbard airport weather station. This discrepancy in reported temperature is comparatively negligible during the winter months when the near-surface temperature is consistently below freezing, reaching -20^{0}C in November and December before being fully sheltered by snow cover January - May. For example, on the 27th of December 2014 the loggers reported a near-surface temperature of -21.47^{0}C, against a measured ambient temperature of -20.4^{0}C. These measured temperatures indicate that temperature ranges in the rock face exceed those measured in ambient temperature, placing considerable stress on the rock surfaces in the transition period from sub-zero to above zero degrees Celcius. Adventfjorden is a brackish environment, where salt levels are negligible due to the high levels of fresh meltwater outflow during the summer and the thick snow ice cover during the winter.

Figure 3: High-resolution near-surface temperature data August 2014 - August 2015

The site is highly active, evidenced by the volume of material accumulated at the bottom of the slope. In fact, 1 by 1 meter sediment traps that had been installed in June 2002 had completely filled up and become difficult to find under the layers of rock debris. The protruding sandstone beds indicate the shale beds are subjected to higher weathering rates, leaving behind small overhanging sandstone layers. Table 1 shows an overview of the individual sites.

Table 1: Overview of the study sites

Methodology

Site installation and photography

In June 2002 seven squares of grey and blue spray paint measuring 50 x 50 centimetres were applied to the rock surface, leaving no gaps within these squares. Any discontinuities in the paint are therefore attributable to loss of surface material from the rock face.

All seven squares were photographed in August 2015, capturing a total of 13 years and 2 months of weathering. The photos were taken with a Fujifilm FinePix SL300: this is a 14 megapixel bridge SLR camera with a sensor resolution of 4288 x 3216 pixels, and the optical zoom lens was set to the wide setting giving a focal length of

4.3 mm (equivalent to 720 mm on a 35 mm camera) and an aperture of F3.1. Depending on the surface roughness between 7 and 10 photographs were taken of each site, these were taken from a variety of angles from a short distance (approximately 1 m) to ensure uniform coverage of the painted section and to maximise overlap, without the use of a tripod or any other stabilisation aids. This gives a ground sample distance (i.e. the size of the pixel projected to the ground surface) of 1.74 mm. Figure 4 illustrates the rotational movement employed while acquiring the images.

Figure 4: Positioning of camera during image acquisition

This approach purposefully uses a very limited number of images; in areas that are difficult to access room to safely manoeuvre around a rock face can be very limited. This study is therefore used to assess whether a limited number of photos can still be used to help interpret rock face characteristics and weathering behaviour.

Rock surface hardness (RSH) survey

As several studies have demonstrated (see for example Aoki and Matsukura, 2007; Betts and Latta, 2000; McCarroll, 1991; Mol and Viles, 2012), RSH can be used as a key-indicator of the degree of weathering of a surface. In this study, an Equotip 3 with D-type probe was used to map differences in RSH across the experiment sites. This equipment was originally developed for the testing of metals (Viles *et al*, 2011), but is now used in both natural settings (Coombes *et al*, 2013; Pérez Alberti *et al*, 2013) and the built environment (Wilhelm *et al*, 2016). The surface hardness is measured through rebound of a 3 mm diameter spherical tungsten carbide test tip against the rock surface. This tip is mounted in an impact body and impacts under spring force against the test surface from which it rebounds (Verwaal and Mulder, 1993). The velocity before impact (V,) and after impact (V2) are measured automatically and displayed as a ratio (V2/V, × 1000) which is denoted by the unit ‘L’, or Leeb unit (Hack *et al.*, 1993).

As noted by Hansen *et al* (2013) repeated rebound tests at the same location on the rock surface result in artificial increase in rebound strength due to compaction of the surface by the rebound device. To minimise this effect and to avoid artificial compaction of the surface, 10 measurements were taken within a 10 by 10 cm space, but never on the exact same position, after manually cleaning the surface of debris such as mud and grit, deposited by wind and surface runoff. This test was repeated seven times on each site to map variability in RSH, totalling 70 impact measurements per test site. By calculating both the mean value per section measured and the standard deviation, the weathering progression was estimated at all test sites.

Structure from Motion (SfM)

The processing of the photography was carried out using Agisoft Photoscan Professional v 1.2.5 (http://www.agisoft.com/), a commercial software that implements a SfM approach to generate 3D meshes. This is a black-box tool which has some user input into the quality of the automated processing and has the advantage that the images that are input into the software do not need to be from the same distance or have the same scale, as a calibration model is derived directly from each photograph. An individual project was created for each painted section and the following steps were taken. After manual verification of the acquired photographs they were all deemed suitable for inclusion in the photogrammetric model. The photographs were uploaded into PhotoScan and the alignment of the acquired images was performed to ‘high accuracy’ (i.e. using the full resolution of the photographs) using the image matching algorithm within the software for a normal camera model. The SfM algorithm provides the basic geometry/structure of the scene, through the position of the numerous matched features, in addition to camera positions and internal calibration parameters (Mancini *et al*, 2013). The camera calibration parameters were automatically determined for the camera type being used and were held fixed for the processing, with a focal length in x- and y-dimensions (i.e. fx and fy) of 3006.56 pixels, and principal point coordinates of cx 2144 pixels and cy 1608 pixels, with a pixel size of 0.001 mm^2. After image matching and alignment, a sparse 3D point cloud is generated (Figure 5a) and manually checked to ensure that the image matching had aligned the photographs correctly. A geometry was created using ‘Ultra High’ target quality (i.e. full resolution output) to create a final dense point cloud, and then texture was applied (Figure 5b). Image-covered point clouds were generated for visualisation purposes (Figure 5c). A scale was then added to the point cloud to give it a local coordinate system using known distances within the photography; given the small surface area of each of the painted sections it was not possible to acquire coordinates of individual targets across the section, and therefore a measuring tape was positioned along the edges of the section to enable scale parameters to be added along the different axes. The reprojection error was reduced by gradual selection (to remove errors within the original point cloud) and the Optimize Cameras tool ensured accurate alignment of the cameras. The average reprojection error of the projects was 0.757 pixels (i.e. a measure of the relative alignment of the images), with an RMSE of 0.519 mm demonstrating reasonable accuracy between the source and estimated camera coordinates. In the absence of independent check points, to determine the precision of the generated model measurements were taken of known distances within the model and compared the actual distance on the surface. The average for all models was ±0.12 mm (standard deviation of 0.08 mm), which was deemed appropriate for the purpose of this research.

Figure 5: SfM processing workflow using the example of Site 4, (a) sparse 3D point cloud produced in PhotoScan with colours obtained from the photographs, (b) the textured dense 3D point cloud created in Photoscan showing the camera positions (blue squares), (c) the final point cloud with RGB values taken from the original photographs in Photoscan, and (d) the output of the CANUPO classification showing the rock cliff areas which remain painted.

The point cloud was exported in LAS-format into CloudCompare (http://www.cloudcompare.org/), an open source 3D point cloud and mesh processing software, for further analysis. The painted area of each rock face (i.e. the outline from the original 2002 area) were clipped and the CANUPO plugin used to classify the images and extract those rocks that still had a painted surface (Figure 5d); training sets of both the bare rock and painted surface were manually digitised, ensuring that there was clear distinction in the classification behaviour of these, and then the automated classification was carried out using a regular ramp (i.e. the scale values will be regularly sampled inside an interval). Those classified as painted rocks were then extracted and differenced from the original extent of the painted area, and the differences calculated to indicate rates of weathering. CloudCompare was also used to compute the roughness (i.e. fine scale variation in elevation) of the point cloud

(Woodget *et al*, 2016). The surface roughness estimation for each point represents the distance between this point and the best fitting plane computed on its nearest neighbour using a kernel size (the radius of a sphere centred on each point), and has been proven to successfully generate rock roughness values by Mastrorocco *et al* (2016), which can be referred to for further evaluation of the technique. A kernel size of 0.05 m was used for the calculations in this research, this was determined by the point cloud extent and size of the elevation changes within the painted sections. This analysis can provide useful information when trying to identify possible changes of the properties or irregularities of a cliff surface.

Results

Rock surface hardness surveys

Overall site observations, as shown in figure 6, indicate that across all seven tests sites variability is high, not only between the highest and lowest measurement per site (for example Leeb value ranging from 60 to 755 at site 2) but also when upper and lower quartiles, and mean are compared.

Figure 6: Overview of RSH results (Leeb value) on all sites, showing mean and upper quartiles as well as highest and lowest measurement per site (n = 70 per site, n = 490 total).

The general trend indicates that while the average hardness decreases closer to the moisture source, the variability in the measurements, e.g. the spread of measurement values, is higher at the sites with higher average values (sites 1, 2, and 3). This likely reflects the nature of volume loss during surface weathering, for example consistent removal of loose materials through crumbling versus more sporadic larger detachments of heavily weathered material. This hypothesis is explored further in individual site analysis.

Individual site analysis

The high variability in rock surface hardness measurements on each experimental section, as illustrated by figure 6, hints at the differences in behaviour across the experimental sites. RSH has been plotted for each individual site, using ArcGIS.

The scarring pattern on site 1 indicates that blocks are removed in relatively large sections as the sandstone deteriorates sufficiently along pre-existing weaknesses, such as bedding planes and fissures, until the material is no longer sufficiently attached to the subsurface and erodes. This is reflected in the RSH Leeb values measured on site (see figure 7A), which indicate a lower degree of weathering of the sections that have been exposed more recently, as evidenced by the removal of painted surface, towards the bottom of the experimental site, whereas the sections closer to the top of the experimental site show lower surface values and higher variability. These sections retain their paint and are thus likely to have been exposed to weathering processes longer. This staged removal of material appears to migrate across the section, starting with removal of material towards the lower section which then leads to loss of support for the overlying sections. This domino effect will continue until the top of the slope is reached, when the cycle is likely to be repeated again with the now newly exposed surface.

In situ observations of site 2 (figure 7B) indicates that while paint has clearly been removed from the surface this is mostly restricted to the thin layers of surface material, there was no noticeable retreat of the surface aside from the loss of the paint layer on the surface and the thin surface layer to which it was adhered (~1mm). Loss of surface appeared to be predominantly restricted to the shale bands between the sandstone beds. Overall site measurements are relatively low towards the top of the experimental surface (see figure 7B), as indicated by the orange colours) and higher towards the bottom where the sandstone layers thicken.

Site 3 (figure 7C) follows the same pattern observed at site 1, with blocky removal of sandstone dominating the surface loss patterns observed, and very similar Leeb values (predominantly 500 - 600 Leeb, with sections of 250 - 350 around relatively recently exposed sandstone surfaces, as evidenced by the removal of the paint layer). The higher standard deviation values towards the bottom of the site are consistent with the weathering behaviour observed, where measured surfaces are loosening along the bedding planes and exhibit signs of imminent removal. This is a noticeable contrast with site 4 (figure 7D) which exhibits much lower Leeb values (150 to 300 value bands are dominant), reflecting the deteriorating shale that dominates this site. The retreat pattern at site 4 resembles the blocky sandstone, with removal of small blocks of shale from right to left of the experimental site. However, the size of block removal is much smaller, following the thinner bedding planes within the shale.

Sites 5 (figure 7E) is situated in a relatively cohesive section of shale, exhibiting very little loss of material. Surface removal predominantly takes place in the form of small-scale crumbling of the surface. The overall site appears relatively stable, which is reflected in the relatively low standard deviations, although a detaching section (red in figure 7E, Leeb value 150 - 200) lowers the mean site value. This is also reflected in figure 6, where site 5 shows relatively low mean values compared to sites 1 through 3 and comparable to site 4.

While site 6 (figure 7F) appears very active, indicated by the very rough surface area, on closer examination very little of the painted surface appears to have been removed. This is in contrast with relatively low Leeb values, which indicate a deteriorating shale band, as seen at site 4. It is likely that while removal of the surface through erosion is yet to take place, this site has deteriorated and could see removal of the surface, similar to that observed at site 4, in the next few years.

Site 7 (figure 7G) is the most heavily deteriorated site, most of the painted surface has been removed. Remnants of the original painted surface are intermittently visible, leaving a patchy pattern on the rock face. This site is closest to the water source, the run off channel which incises the slope 32cm to the right of the experimental site, and is likely to have exacerbated freeze-thaw weathering.

Figure 7[A]: Site 1 spatial distribution patterns of RSH as well as standard deviation per site, indicating variability in measurements

Figure 7[B]: Site 2 spatial distribution patterns of RSH as well as standard deviation per site, indicating variability in measurements

Figure 7[C]: Site 3 spatial distribution patterns of RSH as well as standard deviation per site, indicating variability in measurements

Figure 7[D]: Site 4 spatial distribution patterns of RSH as well as standard deviation per site, indicating variability in measurements

Figure 7[E]: Site 5 spatial distribution patterns of RSH as well as standard deviation per site, indicating variability in measurements

Figure 7[F]: Site 6 spatial distribution patterns of RSH as well as standard deviation per site, indicating variability in measurements

Figure 7[G]: Site 7 spatial distribution patterns of RSH as well as standard deviation per site, indicating variability in measurements

Overall, the shift from higher Leeb values (greens, noticeable at sites 1 through 3) to lower values (oranges and reds, noticeable at sites 5 through 7), with particularly low values around site 4 indicate shifting weathering patterns as well as the interchanging sandstone and shale layers which are both represented in this experiment. While there appears to be a relationship between proximity to the moisture source and the degree of weathering, it is not possible to prove this conclusively based on Leeb values alone. These preliminary conclusions therefore are here combined with data extracted from the photographs of the painted sections using SfM.

Structure from Motion results

As the Leeb values by themselves were not conclusive, as indicated in the previous section, additional analysis was carried out using SfM. The SfM enabled calculation of the change in painted area in 2015 compared to the original spray painted extent, these are shown in Table 2. All sites experienced a reduction in the areal extent of the painted sections over the study period, with Sites 2, 4 and 7 recording the largest difference (see table 2). This is not consistent with the Leeb value measurement observations, which showed the lowest values in sites 5 through 7.

Table 2: Areal change in coverage of the painted area and calculated weathering rate over the period of observation extracted from the SfM point clouds

To further investigate the potential of photogrammetric analysis as a tool for weathering studies, the surface roughness values were extracted using CloudCompare. The roughness data extracted from the rock sections is related to the magnitude and frequency of surface height fluctuations from a fixed datum measured in metres; thus where surfaces have a low height difference between features and small number of irregularities across the area this equates to a low surface roughness (Hollaus *et al*, 2014). *In situ* observations of the plots (figure 8) indicate that surface roughness varies across the sites. For example, site 4 exhibits higher roughness measurements (indicated by greens and yellows) than site 5 where lower roughness values (indicated by blues) appear dominant.

Figure 8: Surface roughness calculated in CloudCompare for (a) Site 1: mean roughness (Ra) = 0.00092 m, (b) Site 2: Ra = 0.00093 m, (c) Site 3: Ra = 0.00088 m, (d) Site 4: Ra = 0.001 m, (e) Site 5: Ra = 0.00078 m, (f) Site 6: Ra = 0.00096 m, and (g) Site 7: Ra = 0.00097 m.

A quantitative analysis of these surfaces (figure 9A) shows that sites can be placed in order of roughness, based on the percentage cover of the highest and lowest roughness values. As shown in figure 9B, site 5 exhibits the highest peak of low-roughness values (0.001 m), showing an overall smoother surface than that of site 4 (figure 9C), which has the highest frequency of high-roughness values (0.0025 m and above) on its surface. This confirms the *in situ* observations that site 5 is dominated by slow crumbling of the surface, with minimal surface volume loss, whereas site 4 which is dominated by fractured, actively weathering shale which is released from the surface in small block (cms) rather than powder (mms) volumes. This approach therefore provides a means of converting visual field observations through digital photos into a quantitative data for investigating site behaviour.

Figure 9: Surface roughness plotted against the percentage of the total site surface for (A) all of the sites, (B) Site 5, (C) Site 4

Using the quantitative ranking provided by the surface roughness measurements the sites are placed in order of roughness and plotted against the percentage surface roughness (figure 10). Overall there appears to be a relationship between surface roughness and surface loss, which is divided according to lithology; the sandstone loses relatively less material and exhibits a smoother surface due to the resistance of the bands to weathering processes. The shale, in contrast, exhibits very high surface loss in combination with high site roughness. The exceptions to this are sites 5 and 6 (crumbling shale), which both exhibit relatively little surface loss, even though site 6 measures higher surface roughness. This is likely due to the placement of site 6 within the runoff channel where freeze thaw exploitation of fractures is likely have exacerbated roughness through the exploitation of fractures and joints.

Figure 10: Site roughness plotted against the percentage surface loss. Linear trend line added to emphasise the difference in behaviour of the sandstone, which loses volume in larger blocks leading to lower surface roughness, compared to the active shale where volume is lost through small block removal, leading to a irregularly shaped surface morphometry.

Discussion

The results presented in this paper have demonstrated that individually the surface hardness measurements and photogrammetric measurements extracted using SfM can be informative of the general condition of a site. However, neither set of results were entirely conclusive. Therefore, to enhance interpretation and test the viability of photogrammetry and SfM analysis as a low-cost contribution to weathering studies, the results have been combined. When plotting the average surface hardness (Leeb values) and the variability in RSH (Leeb value standard deviation) with the surface loss percentage data obtained through SfM analysis three main clusters emerge (see figure 11). The grouping of the more resistant shale of sites 5 and 6, the sandstone which predominantly loses volume through blocky removal along pre-existing weaknesses retains its higher Leeb value as would be expected from a more resistant rock, but exhibits high variability (standard deviation) as individual segments and blocks deteriorate before removal. Where shale is part of the experimental site lithology the variability decreases as well as the overall surface hardness, which conforms with the small-scale removal of sediment from the surface observed *in situ*.

The third cluster is the actively weathering shale (site 4 and 7), which crumbles in small blocks and results in lower RSH values across the experimental site.

Figure 11: Weathering variability (standard deviation) plotted against site surface loss [top], and average RSH (leeb value) plotted against site surface loss [bottom]. The polynomial trendline (order 2) emphasises the clustering of the lithologies.

As figure 11 demonstrates, there is a non-linear link between the surface loss percentage and the measurements obtained by the RSH. Both the standard deviation and average RSH measurement show similar patterns, namely that the more resistant shale bands are relatively resistant to weathering, despite their comparatively low rock surface hardness values, and are uniform.

The sandstone sites, in contrast, consist of more weathering resistant material that is removed from the surface in small blocks. This leads to an overall higher rock surface hardness, but variability is caused by sections that are detaching (low rock surface hardness readings) within the same measurement area as those that are still fully attached to the underlying rock mass (high rock surface hardness readings). The active crumbling shale sites experienced the highest overall surface removal rates but registered low rock surface hardness values with little variation. By combining rock surface hardness with the simplified SfM approached used in this study we can therefore provide quantitative answers to not only the question of how hard a rock surface is, implied to correlate to a rock surface resistance to weathering processes (Aoki and Matsukura, 2007), but also the morphology of material removal from the surface. We can distinguish between surface removal rates at similar lithologies, for example the shale bands, but it can also help to understand areas of larger variability, such as observed in the sandstone bands.

Application of SfM in this research has enabled quantitative data to be derived on both surface deterioration and roughness values, which has supplemented traditional rock weathering techniques and allowed a site that was established prior to the advent of this method to be measured in this way. The data collection for SfM is light-weight, portable and low-cost, requiring only a camera; depending on the requirements of the project the model and associated expense of this can vary, but this research has demonstrated the potential when using a low-cost consumer grade camera. To achieve successful processing the photographs need to be obtained from multiple angles and cover the entire feature of interest, this will allow the image matching software to achieve the best results. And as has been demonstrated in this study, when working in remote and potentially dangerous sites, where safety and/or inaccessibility prevents acquisition of images from different vertical angles the technique can still be utilised to produce surface reconstructions using multiple angles along the same horizontal plane. SfM software can adjust for variation in the distance between the camera and the object, but it is best to try and standardise this as much as possible to avoid trying to merge photographs of different scales and use a fixed camera lens rather than zooming in from certain angles. Ground control points are required to provide a known scale for the 3D point cloud; these can be identifiable features within the image that have a measured coordinate, targets that have been placed for this purpose or a known scale that is placed within the field of view.

The use of combined surface loss and rock surface hardness allows for identification of both lithological characteristics and weathering behaviour within that lithology. In complex lithology areas, i.e. banded stratigraphies comprising multiple lithologies of variable friability, these new insights can aid in identifying spatial changes in individual band behaviour, and to relative weathering rate interpretations. Using traditional destructive methods, such as thin section analysis, and additional non-destructive methods, such as permeametry and UPV, could eventually have displayed a similar clustering behaviour, this method is shown to provide a viable supporting dataset for weathering behaviour interpretation. The SfM, together with RSH, correctly identifies the different lithologies and supports differential weathering behaviour interpretation. In areas where the stone type is heavily altered by diagenesis, chemical weathering or metamorphosis and difficult to identify this could be a valuable new approach in identifying lithologies according to their weathering behaviour; an approach that has not yet been employed.

The use of SfM demonstrated in this research has very good potential for further integration into rock weathering studies; the equipment is commercially available, portable and relatively affordable. This is particularly useful in complex lithology field settings which are difficult to access. The use of visual control point identification avoids the need to transport a tripod or other cumbersome equipment, and circumvents the issue of attaching reflective points, needed for laser scanning, to a friable surface. In combination with the portable non-destructive equipment demonstrated here, this technique can provide a viable support methodology; reducing the time needed in the field to acquire photogrammetric data will enhance the opportunity to successfully enable data and image acquisition in challenging environments, when compared to those methods that require longer in-field run time such as LiDAR scanning. The size of the initial files (i.e. the jpegs generated by the camera, which usually run into megabits rather than gigabits) facilitates easy sharing of data with students and colleagues alike.

Conclusions

As illustrated by this research, the use of photogrammetry and SfM processing can be a viable tool in the 'toolbox' of portable field methods for weathering studies. It is particularly successful in its application in combination with tried and tested field methods such as rock surface hardness. The results here have demonstrated that using the surface hardness and RSH collected using standard field protocols with surface loss and roughness calculations derived from SfM analysis has yielded additional information on the weathering characteristics of the sites under investigation, and enabled the clustering of sites relating their lithology to weathering rates and patterns. The use of commercially available cameras and software, which were used in this research, ensure that this method is accessible to a wide range of researchers and students for both teaching and research, as well as being portable and easy to carry during field work. While this method has previously been applied to larger landscape scale research projects it is demonstrated here that this method can also be applied to small scale weathering processes and can aid in identifying different lithological behaviours within complex composite bands of sedimentary stone.

Acknowledgements

The authors want to thank Angelique Prick (Tromsø University) for her generous sharing of baseline field data and the use of her field sites. The authors thank all staff at UNIS for their help in facilitating the fieldwork. In particular they want to thank Dr Hanne Christiansen and Dr Aga Nowak for the assistance and encouragement. Finally, they thank Dr Mark Williams and Ms Jen Pinnion for their invaluable assistance in the field.

Declaration of competing interests

The authors declared no potential conflicts of interest with respect to the research, authorship, and/or publication of this article.

Funding

The following funds made this fieldwork possible: Research Council of Norway AFG RiS grant 10010; The Robert Scott Memorial Award (2014), Geological Society of London; Small Research Grant (2015), Royal Geographical Society.

References

Adams J and Chandler J (2002) Evaluation of Lidar and medium scale photogrammetry for detecting soft-cliff coastal change. *The Photogrammetric Record* 17(99): 405-418.

Aoki H and Matsukura Y (2007) A new technique for non-destructive field measurement of rock-surface strength: an application of the Equotip hardness tester to weathering studies. *Earth Surface Processes and Landforms* 32(12): 1759-1769.

Barker R, Dixon L and Hooke J (1997) Use of terrestrial photogrammetry for monitoring and measuring bank erosion. *Earth Surface Processes and Landforms* 22(13): 1217-1227.

Barry P and Coakley R (2013) Field test accuracy test of RPAS photogrammetry. *International Archives of the Photogrammetry, Remote Sensing and Spatial Information Sciences* XL-1/W2: 27-31.

Betts MW and Latta MA (2000) Rock surface hardness as an indication of exposure age: An archaeological application of the Schmidt Hammer. *Archaeometry* 42(1): 209-223.

Bourke M, Viles H, Nicoli J, Lyew-Ayee P, Ghent R and Holmlund J (2008) Innovative applications of laser scanning and rapid prototype printing to rock breakdown experiments. *Earth Surface Processes and Landforms* 33: 1614-1621.

Brasington J (2003) Close range digital photogrammetry analysis of experimental drainage basin evolution. *Earth Surface Processes and Landforms* 28(3): 231-247.

Cook KL (2017) An evaluation of the effectiveness of low-cost UAVs and structure from motion for geomorphic change detection. *Geomorphology* 278: 195-208.

Coombes MA, Feal-Pérez A, Naylor LA and Wilhelm K (2013) A non-destructive tool for detecting changes in the hardness of engineering materials: Application of the Equotip durometer in the coastal zone. *Engineering Geology* 167: 14-19.

Dietrich JT (2016) Riverscape mapping with helicopter-based Structure-from-Motion photogrammetry. *Geomorphology* 252: 144-157.

Eckerstorfer A and Christiansen HH (2011) Topographical and meteorological control on snow avalanching in the Longyearbyen area, central Svalbard 2006 - 2009. *Geomorphology* 134(3-4): 186-196.

Eklund JA, Zhang H, Viles HA and Curteis T (2013) Using handheld moisture meters on limestone: factors affecting performance and guidelines for best practice. *International Journal of Architectural Heritage* 7(2): 207-224.

Fonstad MA, Dietrich JT, Courville BC, Jensen JL and Carbonneau PE (2013) Topographic structure from motion: a new development in photogrammetric measurement. *Earth Surface Processes and Landforms* 38(4): 421-430.

Gomez-Heras M and Fort R (2007) Patterns of halite (NaCl) crystallisation in building stone conditioned by laboratory heating regimes. *Environmental Geology* 52(2): 259-267.

Hack HRGK, Hingira J and Verwaal W (1993) Determination of discontinuity wall strength by Equotip and ball rebound tests. *International Journal of Rock Mechanics and Mining Sciences & Geomechanics Abstracts* 30(2): 151-155.

Hall K and André M-F (2001) New insights into rock weathering from high-frequency rock temperature data: an Antarctic study of weathering by thermal stress. *Geomorphology* 41(1): 23-35.

Hansen CD, Meiklejohn KI, Nel W, Loubser MJ and Van Der Merwe BJ (2013) Aspect-controlled weathering observed on a blockfield in Dronning Maud Land, Antarctica. *Geografiska Annaler: Series A, Physical Geography* 95(4): 305-313.

Harris C, Kern-Luetschg M, Christiansen HH and Smith F (2011) The role of interannual climate variability in controlling solifluction processes, Endalen, Svalbard. *Permafrost and Periglacial Processes* 22(3): 239-253.

Hollaus M, Milenković M and Pfeifer N (2014) *A Review of Surface Roughness Concepts, Indices and Applications*. Interreg Alpine Space project - NEWFOR Project number 2-3-2-FR.

James MR and Robson S (2012) Straightforward reconstruction of 3D surfaces and topography with a camera: Accuracy and geoscience application. *Journal of Geophysical Research* 117: F03017.

James MR and Robson S (2014) Mitigating systematic error in topographic models derived from UAV and ground-based image networks. *Earth Surface Processes and Landforms* 39: 1413-1420.

Javernick L, Brasington J and Caruso B (2014) Modeling the topography of shallow braided rivers using Structure-from-Motion photogrammetry. *Geomorphology* 213: 166-182.

Mancini F, Dubbini M, Gattelli M, Stecchi F, Fabbri S and Gabbianelli G (2013) Using Unmanned Aerial Vehicles (UAV) for High-Resolution Reconstruction of Topography: The Structure from Motion Approach on Coastal Environments. *Remote Sensing* 5(12): 6880-6898.

Mastrorocco G, Salvini R, Esposito G and Seddaiu M (2016) 3D point cloud analysis for surface roughness measurement: application of UAV photogrammetry. *Rendiconti Online - Società Geologica Italiana* 41: 313-316.

Matsukura Y and Takahashi K (2000) A new technique for rapid and non-destructive measurement of rock-surface moisture content; preliminary application to weathering studies of sandstone blocks. *Engineering Geology* 55(1-2): 113-120.

Matsuoka N (1995) Rock weathering processes and landform development in the Sør Rondane Mountains, Antarctica. *Geomorphology* 12(4): 323-339.

McCarroll D (1991) The schmidt hammer, weathering and rock surface roughness. *Earth Surface Processes and Landforms* 16(5): 477-480.

McKay CP, Molaro JL and Marinova MM (2009) High-frequency rock temperature data from hyper-arid desert environments in the Atacama and the Antarctic Dry Valleys and implications for rock weathering. *Geomorphology* 110(3-4): 182-187.

Micheletti N, Chandler JH and Lane SN (2015) Investigating the geomorphological potential of freely available and accessible structure-from-motion photogrammetry using a smartphone. *Earth Surface Processes and Landforms* 40(4): 473-486.

Mol L and Viles HA (2010) Geoelectric investigations into sandstone moisture regimes: Implications for rock weathering and the deterioration of San Rock Art in the Golden Gate Reserve, South Africa. *Geomorphology* 118(3-4): 280-287.

Mol L and Viles HA (2012) The role of rock surface hardness and internal moisture in tafoni development in sandstone. *Earth Surface Processes and Landforms* 37(3): 301-314.

Pérez Alberti A, Gomes A, Trenhaile A, Oliveira M and Horacio J (2013) Correlating river terrace remnants using an Equotip hardness tester: An example from the Miño River, northwestern Iberian Peninsula. *Geomorphology* 192: 59-70.

Piermattei L, Carturan L and Guarnieri A (2015) Use of terrestrial photogrammetry based on structure-from-motion for mass balance estimation of a small glacier in the Italian alps. *Earth Surface Processes and Landforms* 40(13): 1791-1802.

Schiefer E and Gilbert R (2007) Reconstructing morphometric change in a proglacial landscape using historical aerial photography and automated DEM generation. *Geomorphology* 88(1-2): 167-178.

Smith BJ and McGreevy JP (1988) Contour scaling of a sandstone by salt weathering under simulated hot desert conditions. *Earth Surface Processes and Landforms* 13(8): 697-705.

Smith MW and Vericat D (2015) From experimental plots to experimental landscapes: topography, erosion and deposition in sub-humid badlands from Structure-from-Motion photogrammetry. *Earth Surface Processes and Landforms* 40(12): 1656-1671.

Smith MW, Carrivick JL and Quincey DJ (2016) Structure from motion photogrammetry in physical geography. *Progress in Physical Geography* 40(2): 247-275.

Sumner PD, Nel W and Hedding DW (2004) Thermal attributes of rock weathering: Zonal or azonal? A comparison of rock temperatures in different environments. *Polar Geography* 28(2): 79-92.

Tonkin TN and Midgley NG (2016) Ground-control networks for image based surface reconstruction: An investigation of optimum survey designs using UAV derived imagery and Structure-from-Motion photogrammetry. *Remote Sensing* 8: 786.

Tonkin TN, Midgley NG, Graham DJ and Labadz JC (2014) The potential of small unmanned aircraft systems and structure-from-motion for topographic surveys: A test of emerging integrated approaches at Cwm Idwal, North Wales. *Geomorphology* 226: 35-43.

Verwaal W and Mulder A (1993) Estimating rock strength with the Equotip hardness tester. *International Journal of Rock Mechanics and Mining Science & Geomechanics Abstracts* 30(6): 659-662.

Viles H, Goudie A, Grab S and Lalley J (2011) The use of the Schmidt Hammer and Equotip for rock hardness assessment in geomorphology and heritage science: A comparative analysis. *Earth Surface Processes and Landforms* 36(3): 320-333.

Westaway RM, Lane SN and Hicks DM (2000) The development of an automated correction procedure for digital photogrammetry for the study of wide, shallow, gravel-bed rivers. *Earth Surface Processes and Landforms* 25(2): 209-226.

Westoby MJ, Brasington J, Glasser NF, Hambrey MJ and Reynolds JM (2012) ‘Structure-from-Motion’ photogrammetry: A low-cost, effective tool for geoscience applications. *Geomorphology* 179: 300-314.

Westoby MJ, Dunning S, Woodward J and Sugden D (2015) Sedimentological characterization of Antarctic moraines using UAVs and Structure-from-Motion photogrammetry. *Journal of Glaciology* 61(230): 1088-1102.

Wilhelm K, Viles H and Burke Ó (2016) Low impact surface hardness testing (Equotip) on porous surfaces - advances in methodology with implications for rock weathering and stone deterioration research. *Earth Surface Processes and Landforms* 41(8): 1027-1038.

Williams RD, Tooth S and Gibson M (2017) The sky is the limit: reconstructing physical geography from an aerial perspective. *Journal of Geography in Higher Education* 41(1): 134-146.

Woodget A, Visser F, Maddock I and Carbonneau P (2016) The accuracy and reliability of traditional surface flow type mapping: Is it time for a new method of characterising physical river habitat? *River Research and Applications* 32(9): 1902-1914.

Zhu L-P, Wang J-C and Li B-Y (2003) The impact of solar radiation upon rock weathering at low temperature: a laboratory study. *Permafrost and Periglacial Processes* 14(1): 61-67.

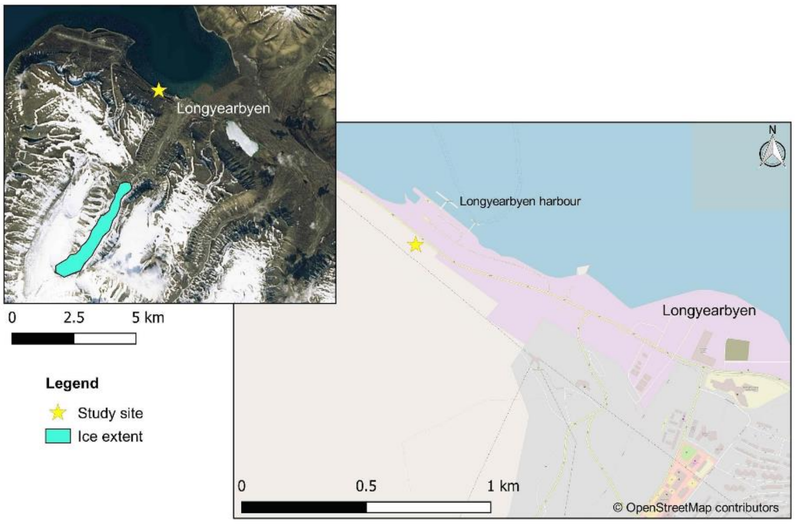

Figure 1: Location map showing the study site (indicated by a star) new Longyearbyen, Svalbard

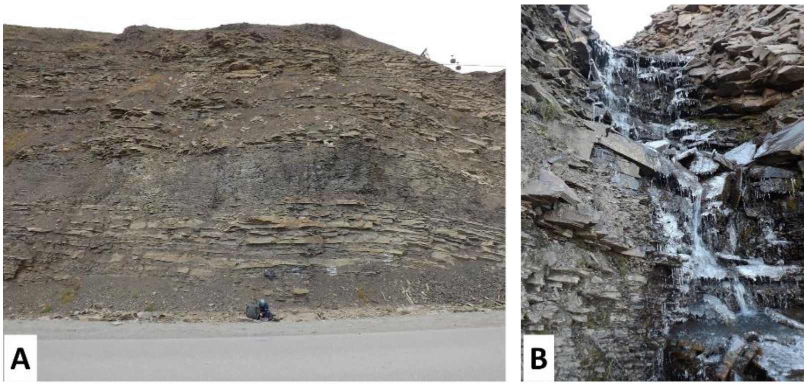

Figure 2: [A] Overview photo of the experimental site, [B] water runoff channel, includes sites 6 and 7

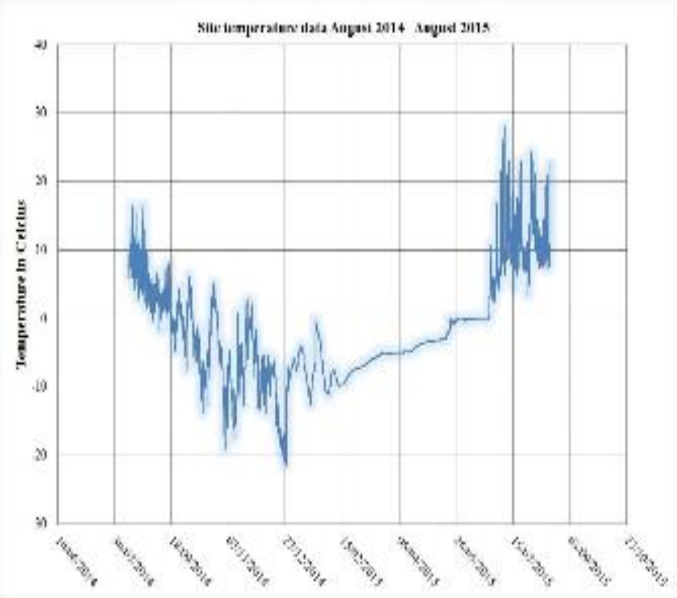

Figure 3: High-resolution near-surface temperature data August 2014 - August 2015

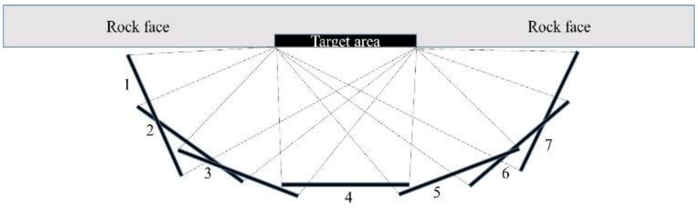

Figure 4: Positioning of camera during image acquisition

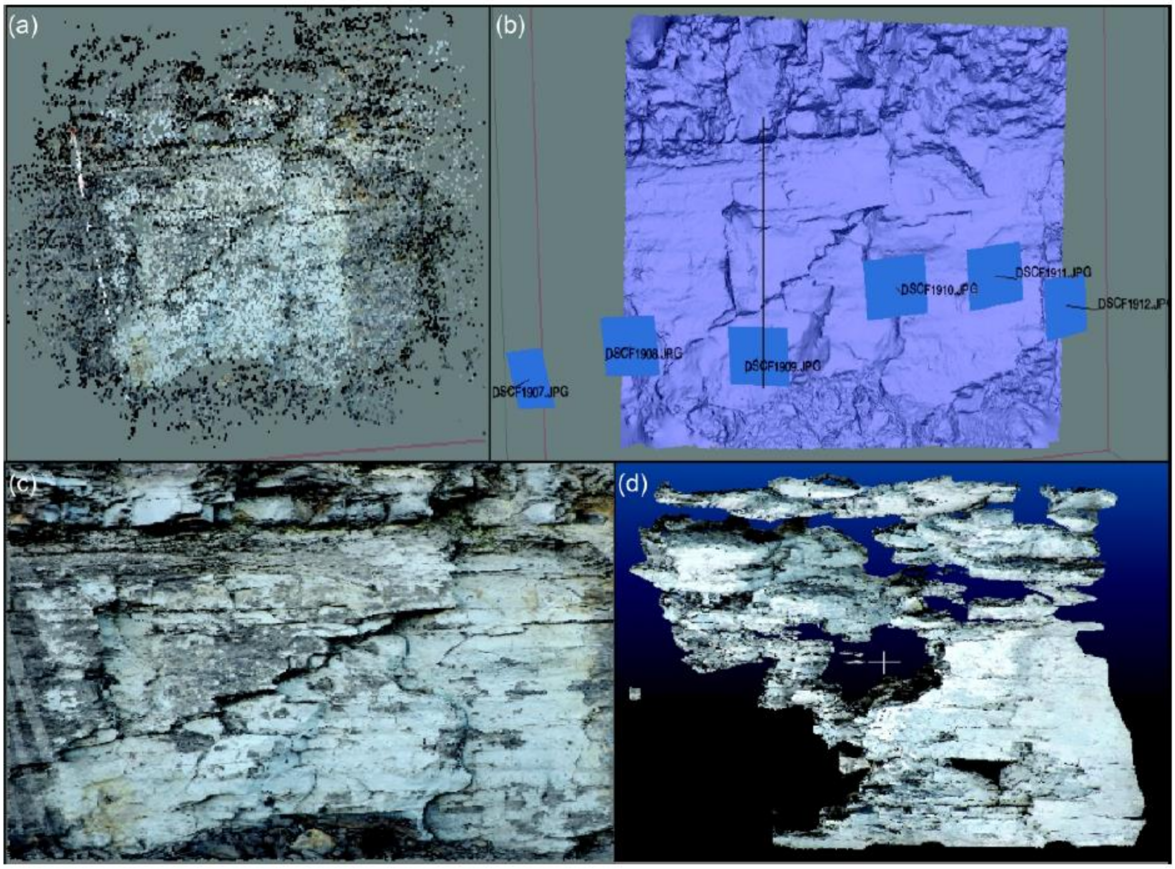

Figure 5. SfM processing workflow using the example of Site 4, (a) sparse 3D point cloud produced in PhotoScan with colours obtained from the photographs, (b) the textured dense 3D point cloud created in Photoscan showing the camera positions (blue squares), (c) the final point cloud with RGB values taken from the original photographs in Photoscan, and (d) the output of the CANUPO classification showing the rock cliff areas which remain painted.

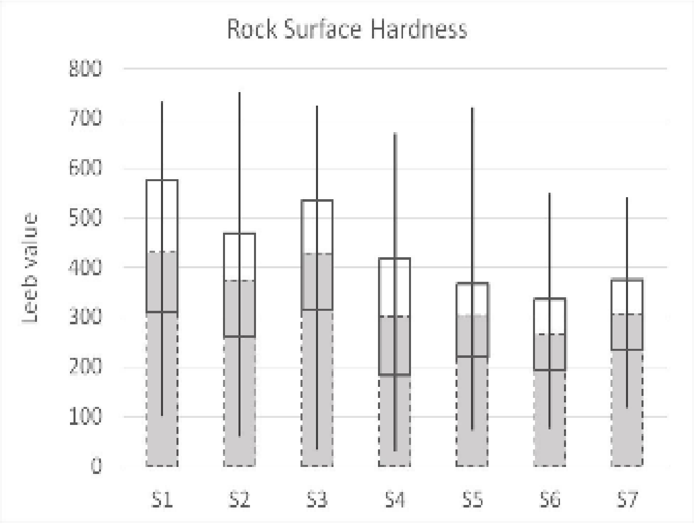

Figure 6: Overview of RSH results (Leeb value) on all sites, showing mean and upper quartiles as well as highest and lowest measurement per site (n = 70 per site, n = 490 total).

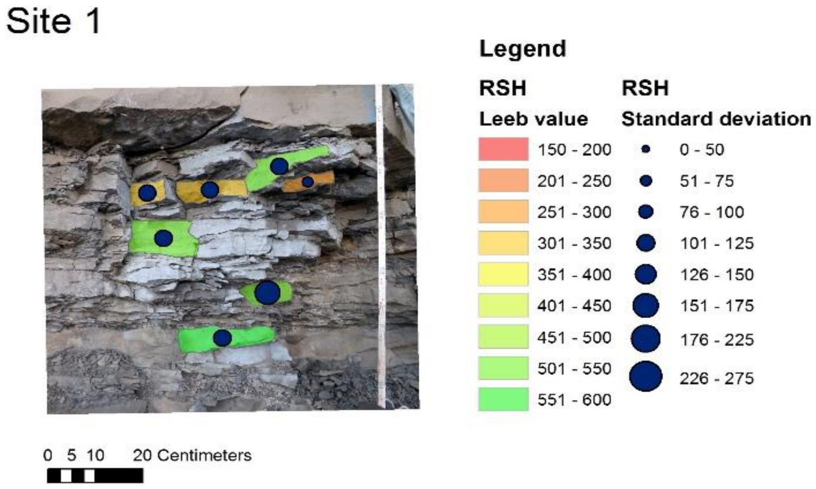

Figure 7[A]: Site 1 spatial distribution patterns of RSH as well as standard deviation per site, indicating variability in measurements

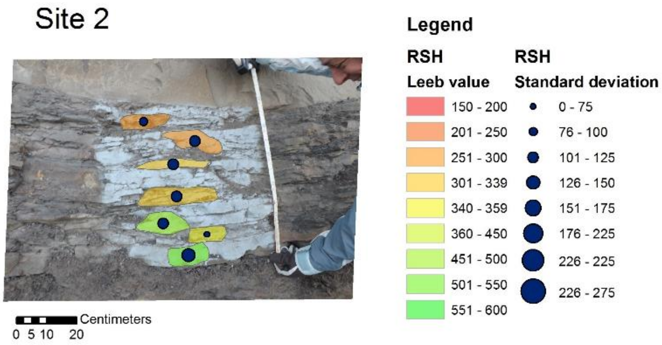

Figure 7[B]: Site 2 spatial distribution patterns of RSH as well as standard deviation per site, indicating variability in measurements

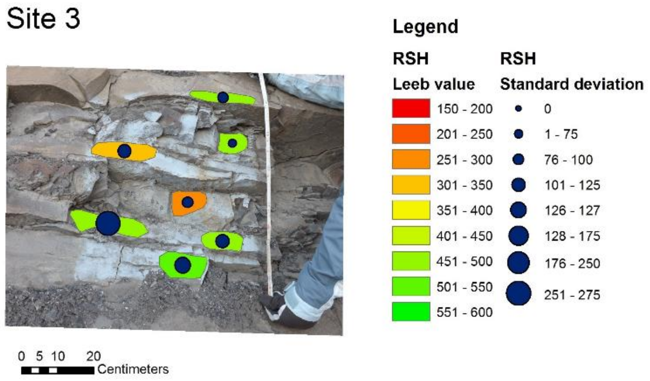

Figure 7[C]: Site 3 spatial distribution patterns of RSH as well as standard deviation per site, indicating variability in measurements

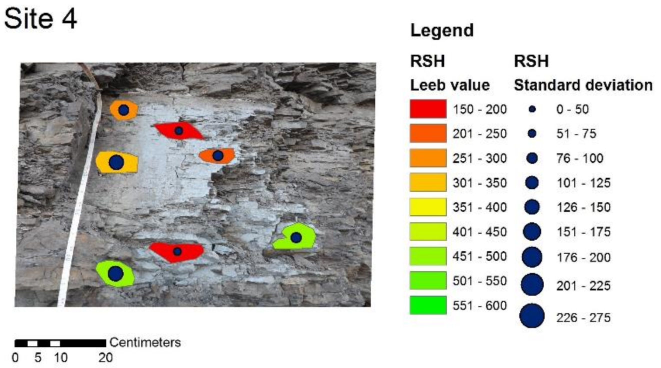

Figure 7[D]: Site 4 spatial distribution patterns of RSH as well as standard deviation per site, indicating variability in measurements

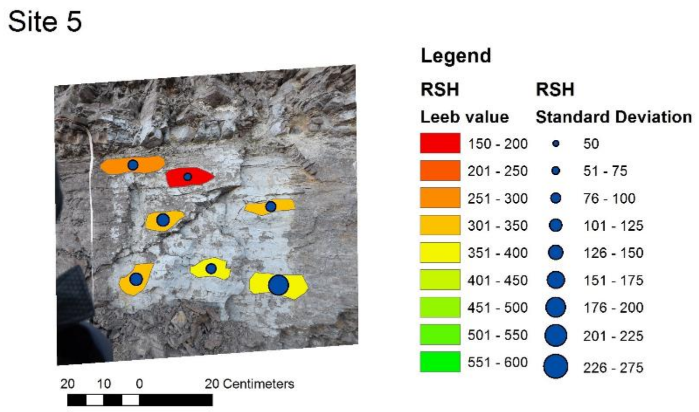

Figure 7[E]: Site 5 spatial distribution patterns of RSH as well as standard deviation per site, indicating variability in measurements

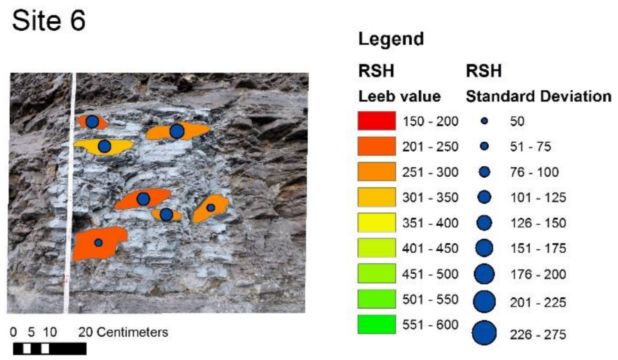

Figure 7[F]: Site 6 spatial distribution patterns of RSH as well as standard deviation per site, indicating variability in measurements

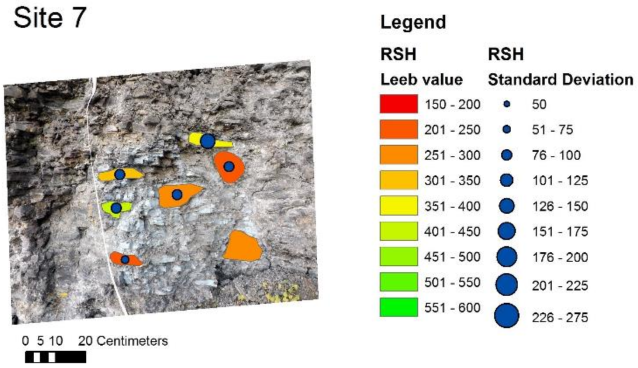

Figure 7[G]: Site 7 spatial distribution patterns of RSH as well as standard deviation per site, indicating variability in measurements

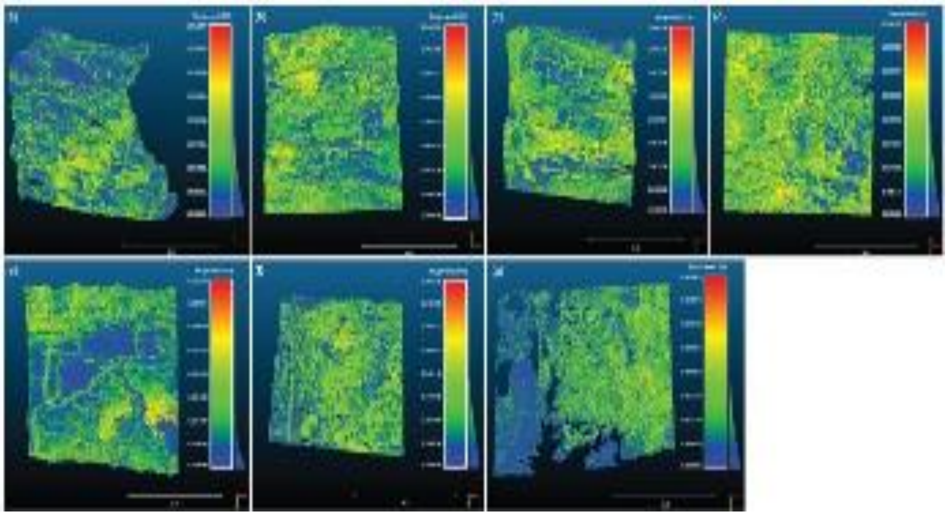

Figure 8: Surface roughness calculated in CloudCompare using a kernel size of 0.05m for (a) Site 1: mean roughness (Ra) = 0.00092 m, (b) Site 2: Ra = 0.00093 m, (c) Site 3: Ra = 0.00088 m, (d) Site 4: Ra = 0.001 m, (e) Site 5: Ra = 0.00078 m, (f) Site 6: Ra = 0.00096 m, and (g) Site 7: Ra = 0.00097 m.

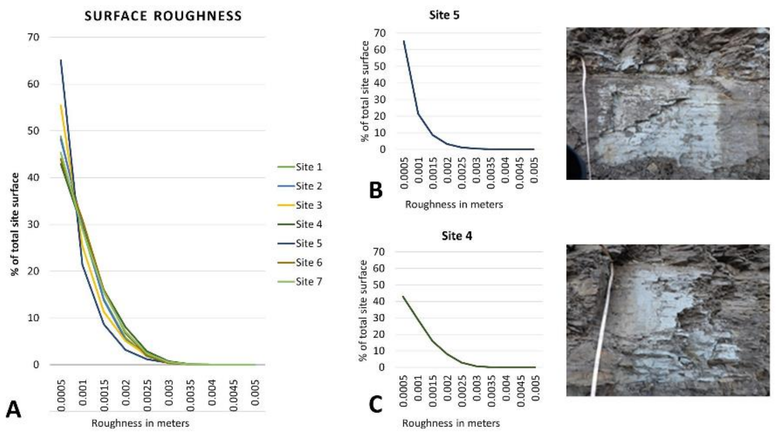

Figure 9: Surface roughness plotted against the percentage of the total site surface for (A) all of the sites, (B) Site 5, (C) Site 4

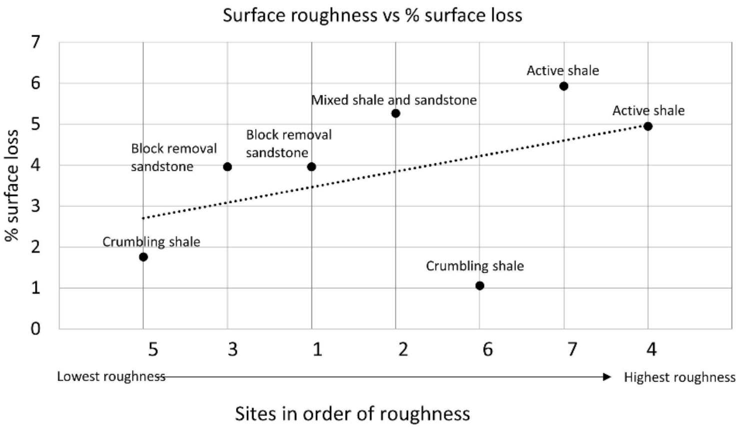

Figure 10: Site roughness plotted against the percentage surface loss. Linear trend line added to emphasise the difference in behaviour of the sandstone, which loses volume in larger blocks leading to lower surface roughness, compared to the active shale where volume is lost through small block removal, leading to a irregularly shaped surface morphometry

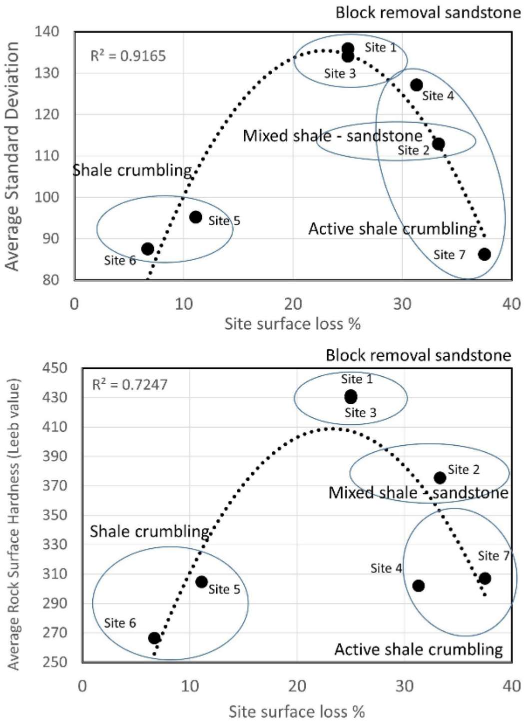

Figure 11: Weathering variability (standard deviation) plotted against site surface loss [top], and average RSH (leeb value) plotted against site surface loss [bottom]. The polynomial trendline (order 2) emphasises the clustering of the lithologies.

Site no		Description
1		Predominantly based in thin-bedded sandstone, interlayered with shale. Both the shale beds and the surrounding sandstone showed clear loss of surface material, though a decrease in loss in the beds directly sheltered by the less friable sandstone bed overlying the site.
2	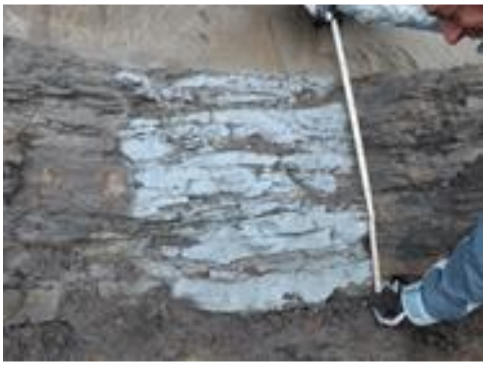	Thin sandstone beds with interbedded shale layers, which are relatively thin (3-5 cm). Some evidence of large-scale loss of surface. Sandstone appears to largely be intact, some shale surface loss, especially near the boundaries with the sandstone layer.
3		Blocky sandstone dominates this site, with larger section removal where sections of the sandstone have dislodged from the rock face. The preferential removal of the shale appears to lead to a loss of sandstone along vertical joints.
4		This site is composed entirely of shale, leading to removal of material in smaller volume section than those observed in sandstone. The weathering front appears to move from right to left (see image). This follows on from an earlier removal episode which

		followed the same pattern and exposed the surface currently weathering.
5		Thinly-bedded shale site, showing gradual crumbling of rock face towards the upper left side of the experimental site. Field observations indicate gradual granular detachment of the surface layer, in contrast with sites 1 and 3.
6	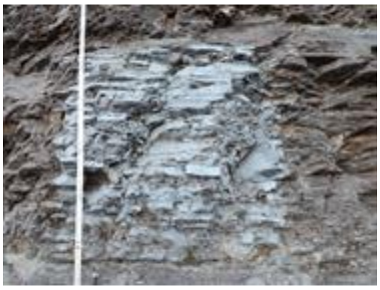	Similar to site 4, this site is situated entirely across a shale bed, exhibiting the same small-volume loss of material. However, there is an absence of a clear weathering front, as removal seems to be taking place uniformly across the experimental surface. This site is within the runoff channel and in close proximity to high moisture levels.
7		This site is adjacent to the moisture source, within the runoff channel which runs from the higher slopes down to the road. Area size of removed painted surface indicates this is the most actively weathering site.

Table 1: Overview of RSH results (Leeb value) on all sites, showing mean and upper quartiles as well as highest and lowest measurement per site (n = 70 per site, n = 490 total).

	Percentage change in coverage of painted area	**Weathering rate per month since 2002 (cm2)**
Site 1	-25.0%	3.96
Site 2	-33.3%	5.27
Site 3	-25.0%	3.96
Site 4	-31.3%	4.95
Site 5	-11.1%	1.76
Site 6	-6.7%	1.06
Site 7	-37.5%	5.93

Table 2: Areal change in coverage of the painted area and calculated weathering rate over the period of observation extracted from the SfM point clouds